

Effect of Manganese Valence on Specific Capacitance in Supercapacitors of Manganese Oxide Microspheres

Xing Chen^{+, [a, b]}, Lei Li^{+, [a]}, Xiaoli Wang,^[c] Kun Xie,^[b] and Yuqiao Wang^{*[a]}

Abstract: Manganese oxides have attracted great interest in electrochemical energy storage due to high theoretical specific capacitance and abundant valence states. The multiple valence states in the redox reactions are beneficial for enhancing the electrochemical properties. Herein, three manganese microspheres were prepared by a one-pot hydrothermal method and subsequent calcination at different temperatures using carbon spheres as templates. The trivalent manganese of Mn₂O₃ exhibited multiple redox

transitions of Mn³⁺/Mn²⁺ and Mn⁴⁺/Mn³⁺ during the intercalation/deintercalation of electrolyte ions. The possible redox reactions of Mn₂O₃ were proposed based on the cyclic voltammetry and differential pulse voltammogram results. Mn₂O₃ microsphere integrated the advantages of multiple redox couples and unique structure, demonstrating a high specific capacitance and long cycling stability. The symmetric Mn₂O₃//Mn₂O₃ device yielded a maximum energy density of 29.3 Wh kg⁻¹ at 250 W kg⁻¹.

Introduction

Manganese oxides have attracted considerable interest as electrode materials for supercapacitors due to their high theoretical capacity, abundant raw materials and nontoxicity.^[1] In general, the manganese oxides store charges through the valence state transition between Mn(IV) and Mn(III) by intercalation/deintercalation electrolyte ions into the electrode materials.^[2] However, manganese oxides commonly exhibit electrochemically inactive in neutral electrolyte, leading to low specific capacitance.^[3] The main reason can be ascribed to the intercalation/deintercalation of electrolyte ions only on the surface without effective utilization of the Mn(IV)/Mn(III) redox couple. This means that the intercalation/deintercalation reactions only occur on the surface and the bulk of the electroactive materials contributes little to the total capacitance. It is well known that the neutral aqueous electrolyte is promising in portable and wearable electronic devices due to their safeties and electrochemical stabilities.^[4] Therefore, it is critical to

improving the electrochemical properties of manganese oxides in neutral electrolyte.

The manganese valence plays an important role in the intercalation/deintercalation redox reactions. As is well known, the redox couple of Mnⁿ⁺/Mn⁽ⁿ⁻¹⁾⁺ can contribute most to the total capacitance. For instance, Mn₃O₄/MnO₂-NG with mixed-valence state cations was favorable for the formation of ion and electron defects, leading to excellent electrochemical properties.^[5] Besides, the core/shell a-Mn₂O₃@a-MnO₂ exhibited more redox couples of Mn (Mn³⁺/Mn²⁺ and Mn⁴⁺/Mn³⁺) instead of single manganese oxide.^[6] As an intermediate valence, the trivalent manganese possesses two pair redox couples of Mn³⁺/Mn²⁺ and Mn⁴⁺/Mn³⁺.^[7] The reversible transition of Mn³⁺/Mn²⁺ and Mn⁴⁺/Mn³⁺ redox couples originated from the intercalation/deintercalation of electrolyte ions can enhance the specific capacitances of manganese oxides. Notably, the trivalent manganese in NiCo-LDH can facilitate the rapid and effective transition of Mn²⁺/Mn⁴⁺ redox couple, further enhancing the redox reaction activity and reversibility.^[8] Therefore, the trivalent manganese with two redox couples of Mn²⁺/Mn³⁺ and Mn³⁺/Mn⁴⁺ is expected to maximize the degree of redox reactions, leading to superior specific capacitance.

The morphologies of the electroactive materials also play an important role in the intercalation/deintercalation redox reactions. A well-defined nano/microstructure with a large surface area and a porous structure can expose more electroactive sites and facilitate better electrolyte ions accessibility into the inner surface of active materials. Recently, 3D hierarchical nano/microspheres have gained ever-increasing interest as a special type of nano/microstructures. The unique structures can integrate the merits of nanostructures and microstructures, providing short electron/ion diffusion channels, large specific surface area and more exposed electrochemical sites.^[9] However, exploiting a facile method to prepare the hierarchical manganese oxide nano/microsphered is still a challenge.

[a] Dr. X. Chen,⁺ L. Li,⁺ Prof. Y. Wang
School of Chemistry and Chemical Engineering
Southeast University
211189 Nanjing (P. R. China)
E-mail: yqwang@seu.edu.cn

[b] Dr. X. Chen,⁺ Prof. K. Xie
Chongqing Key Laboratory of Water Environment Evolution and Pollution
Control in Three Gorges Reservoir
Chongqing Three Gorges University
404020 Wanzhou (P. R. China)

[c] Dr. X. Wang
College of Optoelectronic Engineering
Chongqing University
400044 Chongqing (P. R. China)

[⁺] These authors contributed equally to this work.

Supporting information for this article is available on the WWW under <https://doi.org/10.1002/chem.202100113>

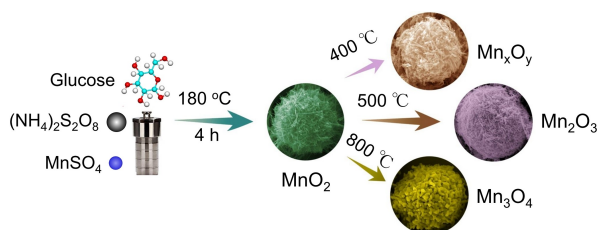
In this work, we reported the preparation of MnO , Mn_2O_3 and Mn_3O_4 microspheres by a one-pot hydrothermal method and subsequent calcination at different temperatures (Scheme 1). The prepared hierarchical manganese oxide microspheres exhibit a similar configuration and size. The unique structures can provide facile diffusion of electrolyte ions, large specific surface area and robust structural stability. For Mn_2O_3 , two redox couples of $\text{Mn}^{3+}/\text{Mn}^{2+}$ and $\text{Mn}^{4+}/\text{Mn}^{3+}$ were involved in the reversible intercalation/deintercalation of sodium cations. The multiple redox transitions of $\text{Mn}^{3+}/\text{Mn}^{2+}$ and $\text{Mn}^{4+}/\text{Mn}^{3+}$ can enhance the specific capacitance of Mn_2O_3 . The possible redox reaction equations of intercalation/deintercalation of sodium cations into Mn_2O_3 were proposed according to the cyclic voltammetry and differential pulse voltammogram results. Mn_2O_3 with multiple redox couples, ordered mesoporous structure and large specific surface area was expected to demonstrate excellent electrochemical performance for supercapacitors.

Results and Discussion

Morphology and structure characterization

The SEM and TEM images show that the carbon sphere possesses a smooth surface with a diameter of about $1.74\ \mu\text{m}$ (Figure 1a1 and b1). MnO_2 microsphere consisted of tiny MnO_2 nanowires on the surface of the carbon sphere (Figure 1a2 and 1b2). Subsequently, Mn_xO_y microsphere was obtained after calcination of MnO_2 at 400°C . Mn_xO_y microsphere maintains the sphere-like structure, which is covered with thread-like nanowires (Figure 1a3 and 1b3). With increasing the calcination temperature to 500°C , the morphology change was observed for Mn_2O_3 sample (Figure 1a4 and Figure 1b4). Numerous interlaced nanorods stacked together to form a porous microsphere. When the temperature was increased to 800°C , numerous worm-like nanoparticles uniformly covered on the surface to assemble Mn_3O_4 microsphere (Figure a5 and b5). MnO_2 , Mn_xO_y , Mn_2O_3 and Mn_3O_4 microspheres exhibited a similar size with an average diameter of $3.62\ \mu\text{m}$.

The XRD diffraction peaks of MnO_2 at 12.3° , 17.7° , 28.4° , 37.3° , 41.8° , 49.5° , 56.1° , 59.7° , 65.1° , 68.8° and 72.6° are indexed to the (110), (200), (310), (211), (301), (411), (600), (521), (002), (541) and (312) planes of the tetragonal MnO_2 phase (JCPDS No. 44-0141), respectively (Figure 2a). However, the diffraction peaks of the carbon are absent, which is probably due to the



Scheme 1. Schematic illustration of manganese oxide microspheres.

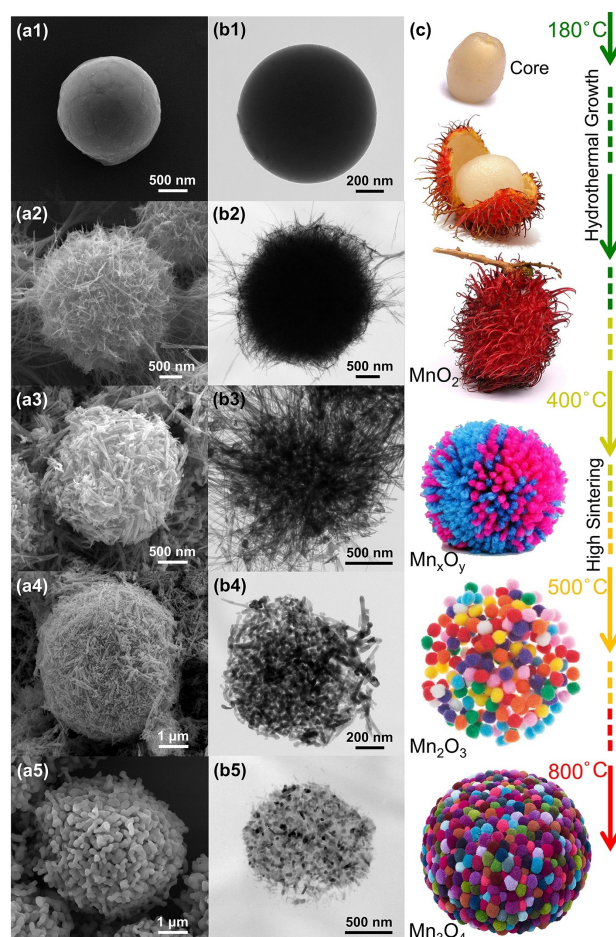


Figure 1. SEM and TEM images of (a1, b1) carbon sphere, (a2, b2) MnO_2 , (a3, b3) Mn_xO_y , (a4, b4) Mn_2O_3 and (a5, b5) Mn_3O_4 ; (c) Schematic diagram of the formation process of MnO_2 , Mn_xO_y , Mn_2O_3 and Mn_3O_4 microspheres.

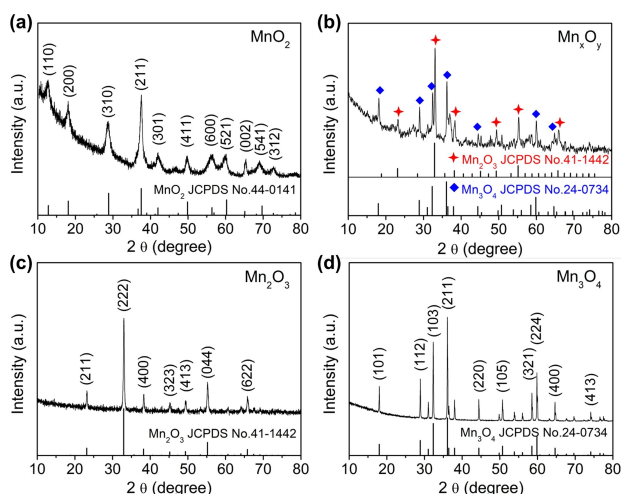


Figure 2. XRD patterns of (a) MnO_2 , (b) Mn_xO_y , (c) Mn_2O_3 and (d) Mn_3O_4 .

low crystallinity and mass loading of the carbon.^[10] For Mn_xO_y (Figure 2b), the diffraction peaks located at 23.1° , 33.0° , 38.4° , 49.4° , 55.1° and 65.9° are assigned to the (211), (222), (400),

(431), (440) and (622) planes of the orthorhombic Mn_2O_3 phase (JCPDS No. 41-1442), whereas the other peaks at 18.1° , 28.9° , 32.4° , 36.3° , 44.5° , 60.0° and 64.6° can be assigned to the (101), (112), (103), (202), (220), (224) and (400) planes of Mn_3O_4 phase (JCPDS No. 24-0734). These results confirm that Mn_xO_y is composed of Mn_2O_3 and Mn_3O_4 phase. For Mn_2O_3 (Figure 2c), the diffraction peaks correspond to the standard orthorhombic Mn_2O_3 (JCPDS No. 41-1442). The dominant diffraction peaks detected in Figure 2d are ascribed to Mn_3O_4 phase (JCPDS No. 24-0734). The crystallite sizes of manganese oxides were estimated by the Scherrer equation from MnO_2 (211), Mn_2O_3 (222) and Mn_3O_4 (211) reflections,^[11] and the corresponding values were approximately 14.9, 29.3 and 55.0 nm, respectively.

The HRTEM image presents the nanowire-structure on the surface of MnO_2 microsphere (Figure 3a) and the corresponding selected area electron diffraction (SAED) pattern exhibits several clear diffraction rings, indexing to the (310), (211), (301) and (411) planes of the tetragonal phase MnO_2 (JCPDS No. 44-0141) (Figure 3b). Figure 3c shows the HRTEM image of Mn_xO_y with distinct lattice fringes. The high-magnification TEM image of the violet dashed circle shows a lattice spacing of 0.67 nm, corresponding to the (011) plane of the cubic Mn_2O_3 phase (Figure 3d). The inverse fast Fourier transform (IFFT) image of the yellow dashed circle displays a lattice fringe spacing of 0.24 nm, assigning to the (004) plane of the tetragonal Mn_3O_4 (Figure 3e). Figure 3f presents the nanorod-like structure of Mn_2O_3 . The high-magnification TEM image of the white dashed square exhibits a lattice fringe spacing of 0.38 nm, corresponding to the (211) plane of the cubic Mn_2O_3 . The diffraction rings of Mn_3O_4 are ascribed to the (100), (102) and (103) planes of the tetragonal Mn_3O_4 (Figure 3h–i).

The possible reaction mechanisms lead to different morphology of Mn-based oxides at different temperatures can be

described as follows: At the beginning of the reaction, Mn^{2+} ions may be adsorbed on the surface of the carbon sphere. Then MnO_2 crystal whiskers are formed and assembled on the surface of the carbon sphere^[12]. During the calcination processes, MnO_2 microspheres will be reduced to different materials under different temperatures^[13]. Simultaneously, CO_3^{2-} and HCO_3^- ions inside the carbon sphere start to decompose and form loose structures. The thread-like Mn_xO_y microspheres are obtained at a low calcination temperature of 400°C . As the temperature is increased to 500°C , the thread-like nanowires are transformed into interlaced nanorods, forming Mn_2O_3 microspheres. When the temperature is increased to 800°C , the interlaced nanorods are changed to worm-like nanoparticles. Mn_3O_4 microspheres are obtained.

As is well known, the specific surface area and pore sizes of the electrodes play a crucial role in enhancing the electrochemical performance. N_2 adsorption/desorption isotherms of Mn_xO_y and Mn_3O_4 show a type III isotherm and the adsorption-desorption isotherms are nearly overlapped, suggesting no evidence of mesopores (Figure 4a). MnO_2 and Mn_2O_3 exhibit a type IV isotherm with a distinct hysteresis loop at the P/P_0 range of 0.4–1.0,^[14] indicating the existence of mesopores. The specific surface area and total pore volumes of MnO_2 , Mn_xO_y , Mn_2O_3 and Mn_3O_4 are presented in Table S1. Mn_2O_3 possesses a higher specific surface area ($141.2\text{ m}^2\text{ g}^{-1}$) and a larger pore volume ($0.38\text{ cm}^3\text{ g}^{-1}$). Additionally, the BJH pore size distribution curves of MnO_2 and Mn_2O_3 exhibit a major peak in the range of 10–40 nm (Figure 4b), verifying the existence of mesoporous structures. Mn_xO_y and Mn_3O_4 samples show no evidence of mesoporous structures. The large surface area, large pore volume and mesoporous structure can expose more electrochemical active sites for charge storage and supply abundant

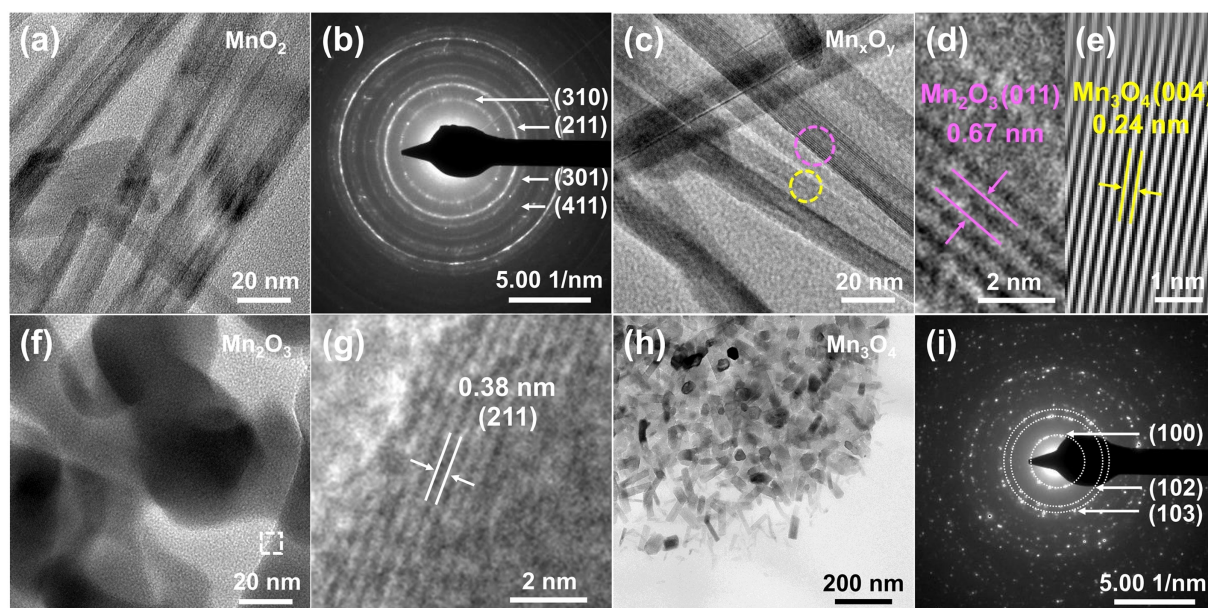


Figure 3. TEM images of (a) MnO_2 , (c) Mn_xO_y , (f) Mn_2O_3 and (h) Mn_3O_4 . The selected area electron diffractions of (b) MnO_2 and (i) Mn_3O_4 . The high-magnification TEM images of (d) Mn_xO_y and (g) Mn_2O_3 . The IFFT image of (e) Mn_xO_y .

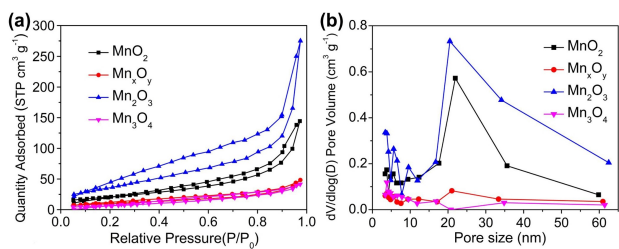


Figure 4. (a) N_2 adsorption/desorption isotherms. (b) The plots of BJH pore size distributions of manganese oxides.

channels for ion and electron transfer, resulting in high specific capacitance.

Electrochemical measurements

The CV curves of MnO_2 , Mn_xO_y and Mn_3O_4 electrodes exhibited a shape of quasi-rectangular, indicating the capacitive behavior (Figure 5a). This was in accordance with the previously reported work that the intercalation/deintercalation redox reactions commonly occurred on the surface of manganese oxides without no obvious redox peaks in Na_2SO_4 electrolyte.^[15] Particularly, a pair of redox peaks obviously appeared in the CV curve of Mn_2O_3 , while no redox peaks were observed in the CV curves of MnO_2 , Mn_xO_y and Mn_3O_4 . The appearance of the redox peaks is mainly due to the redox reactions. The redox peaks originated from the reversible intercalation/deintercalation of sodium cations into the interior of Mn_2O_3 . To explore the specific redox couples in the redox peaks, the DPV measure-

ments were conducted. The DPV curves show two oxidation peaks and two reduction peaks at the amplitude of 50 mV (Figure 5b). Due to the existence of manganese (III) in Mn_2O_3 , the two pairs of redox couples can be ascribed to Mn^{3+}/Mn^{2+} and Mn^{4+}/Mn^{3+} redox couples.^[8] The broad peaks at about 0.31 and 0.83 V can be attributed to the oxidation of Mn^{2+} to Mn^{3+} and Mn^{3+} to Mn^{4+} , respectively. The peaks at 0.78 and 0.30 V can be ascribed to the reduction of Mn^{4+} to Mn^{3+} and Mn^{3+} to Mn^{2+} , respectively. The DPV curves at different amplitudes were also recorded and the corresponding oxidation and reduction peaks still can be observed (Figure 5c). The DPV results provided a convinced confirmation that two pairs of redox couples were involved in the redox reactions. The probable redox reaction equations of Mn_2O_3 were proposed as follows:^[16]



Mn_2O_3 electrode possessed a larger integrated area of CV curves, demonstrating a higher specific capacitance. Additionally, the GCD curves of MnO_2 , Mn_xO_y , Mn_2O_3 and Mn_3O_4 electrodes exhibited a nearly symmetric triangular shape (Figure 5d), illustrating the excellent rate performance and reversibility. Among the four samples, Mn_2O_3 electrode delivered a longer discharge time, manifesting a higher specific capacitance, which was consistent with the CV results. The IR drops of the four electrodes in Figure 5d are mainly due to the high solution resistances^[17].

The CV and GCD curves of Mn_2O_3 electrode were conducted to further investigate the electrochemical properties. When the

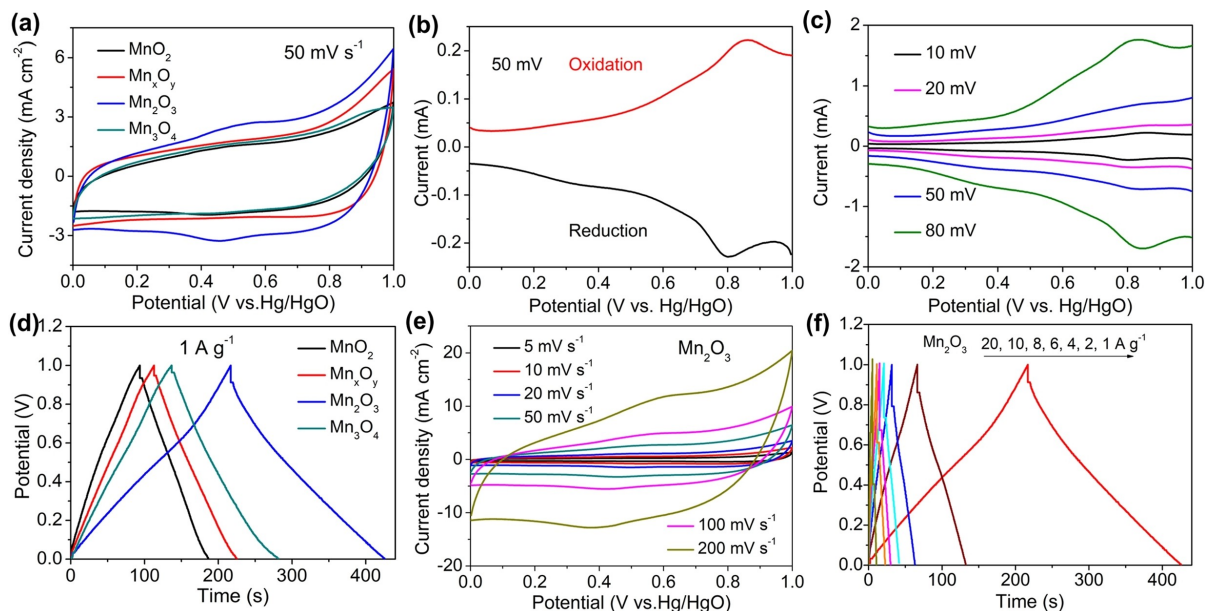


Figure 5. (a) CV curves of manganese oxides at 50 mV s^{-1} . (b) DPV curves of Mn_2O_3 at an amplitude of 50 mV. (c) DPV curves of Mn_2O_3 at different amplitudes. (d) GCD curves of manganese oxides at 1 A g^{-1} ; (e) CV curves of Mn_2O_3 electrode at various scan rates. (f) GCD curves of Mn_2O_3 electrode at various current densities.

scan rate was increased, the oxidation peaks moved to a more positive potential while the reduction peaks shifted to a more negative potential due to the polarization of Mn_2O_3 electrode (Figure 5e). However, the quasi-rectangular shapes of the CV curves were still maintained, demonstrating good electrochemical reversibility and rapid redox reactions. The GCD curves of Mn_2O_3 electrode exhibited nearly symmetric triangular shapes with the increase of current densities, illustrating the high coulombic efficiency during the charge/discharge process (Figure 5f). With the increasing of the current density, the IR drop values increase, which is mainly attributed to the inefficient transmission between electrolyte ions and electrons during the charge/discharge process^[18]. The CV and GCD curves of MnO_2 , Mn_xO_y and Mn_3O_4 electrodes display similar electrochemical characteristics to Mn_2O_3 electrode (Figure S1), exhibiting superior electrochemical performance. According to the calculated specific capacitances, Mn_2O_3 electrode presents higher specific capacitances than those of MnO_2 , Mn_xO_y and Mn_3O_4 electrodes at the same current densities (Figure S2 and Table S2). The specific capacitances of Mn_2O_3 electrode are 209.1, 132.2, 126.4, 123.6, 120.8, 113.0 and 108.0 F g^{-1} at 1, 2, 4, 6, 8, 10 and 20 A g^{-1} , respectively. Mn_2O_3 electrode obtained a high capacitance retention of 51.6% when the current density was increased from 1 to 20 A g^{-1} , demonstrating the superior rate capability. Mn_2O_3 electrode also exhibited a comparable specific capacitance to previously reported works (Table S3).

Basing on the above analyses, the enhanced specific capacitance of Mn_2O_3 electrode can be ascribed to the following reasons: (1) Mn_2O_3 microsphere provided abundant electroactive sites and efficient ion diffusion pathways due to its high specific surface area and unique mesoporous structure. (2) The intermediate valence state of manganese(III) exhibited two redox couples of $\text{Mn}^{3+}/\text{Mn}^{2+}$ and $\text{Mn}^{4+}/\text{Mn}^{3+}$ for the reversible intercalation/deintercalation of sodium cations, resulting in high specific capacitance.

The electrochemical kinetics of the obtained electrodes were investigated by the electrochemical impedance spectroscopy (EIS) measurements. The Nyquist plots were presented in Figure 6a. In the high-frequency region, the intercept on the real axis is related to the solution resistance (R_s), which is composed of the intrinsic resistance of the active materials, the ionic resistance of the electrolyte and the contact resistance between the active materials and the current collector interface.^[19] The diameter of the semicircle represents the

charge transfer resistance (R_{ct}). In the low-frequency region, the straight line represents the Warburg impedance, which is related to the ion diffusion resistance from the electrolyte to the electrode interface.^[20] An equivalent circuit was adopted to simulate the EIS data. The C_{dl} and C_F represent the double-layer capacitance and a Faradaic pseudocapacitor, respectively. The fitted data were shown in Table S4. In comparison with the R_s (2.77 $\Omega \text{ cm}^2$) of MnO_2 electrode, Mn_xO_y , Mn_2O_3 and Mn_3O_4 electrodes exhibited relatively smaller R_s values (1.84, 2.09 and 2.01 $\Omega \cdot \text{cm}^2$, respectively), illustrating the faster charge transfer kinetics. Mn_2O_3 electrode demonstrated a lower R_{ct} value of 0.22 $\Omega \text{ cm}^2$ than those of MnO_2 (0.32 $\Omega \cdot \text{cm}^2$), Mn_xO_y (0.66 $\Omega \text{ cm}^2$) and Mn_3O_4 (0.37 $\Omega \text{ cm}^2$), indicating the efficient charge transport. In the low-frequency region, Mn_2O_3 electrode possessed the lowest Warburg impedance of 0.0068 $\text{S} \cdot \text{sec}^{0.5} \cdot \text{cm}^{-2}$, implying the faster diffusion of the electrolyte ions. The EIS results demonstrate that Mn_2O_3 electrode has better electrical conductivity and faster ion diffusion kinetics.

The long-term cycling stability of the electrode is a critical parameter for practical application. For MnO_2 and Mn_3O_4 electrodes, the initial increase of the specific capacitance in the first 1800 and 1000 cycles may be due to the self-activation process caused by the electrolyte ions diffusion (Figure 6b). The specific capacitances of MnO_2 and Mn_3O_4 electrodes decreased slightly in the subsequent 3200 and 4000 cycles. After 5000 charge/discharge cycles, the capacitance retentions of MnO_2 , Mn_xO_y and Mn_3O_4 electrodes were 100%, 106.2% and 102.2%, respectively. In contrast, Mn_2O_3 electrode maintained a capacitance retention of around 97.6%. It is noteworthy that the specific capacitance of Mn_2O_3 always maintains the maximum value. The excellent cycling stabilities of the four electrodes can be attributed to the unique three-dimensional sphere-like structure, alleviating the volume expansion during the charge-discharge process.

The relationships between the scan rate and current density were used to investigate the reaction kinetics based on equation (3):^[21]

$$i = av^b \quad (3)$$

Where a and b are constants. The value of b is the slope of $\log(i)$ against $\log(v)$. Generally, when the $b=1$, the charge storage process is capacitive-controlled. While the $b=0.5$, it means that the charge storage process is dominated by diffusion-controlled. The calculated b -values of the anodic and cathodic peaks were 0.88 and 0.99, respectively, demonstrating the capacitive-controlled behaviour during the charge-storage process (Figure 7a).

The ratios of the capacitive-controlled and diffusion-controlled processes to the total capacitance for Mn_2O_3 , MnO_2 and Mn_3O_4 electrodes were calculated based on equation (4):^[9a]

$$i(V) = k_1v + k_2v^{1/2} \quad (4)$$

Where $i(V)$ is the current at a certain potential of V , v is the scan rate. k_1 and k_2 correspond to the capacitive-controlled and diffusion-controlled processes, respectively. Figure 7b and Fig-

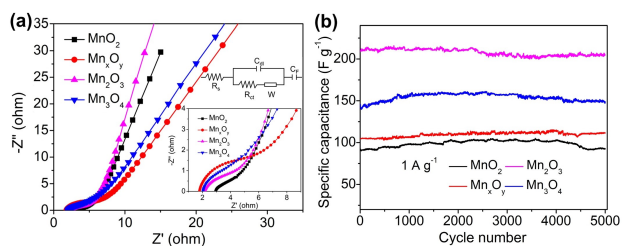


Figure 6. (a) Nyquist plots (insets: the high frequency area enlargement and corresponding equivalent electrical circuit). (b) Cycling performance of manganese oxides at 1 A g^{-1} over 5000 cycles.

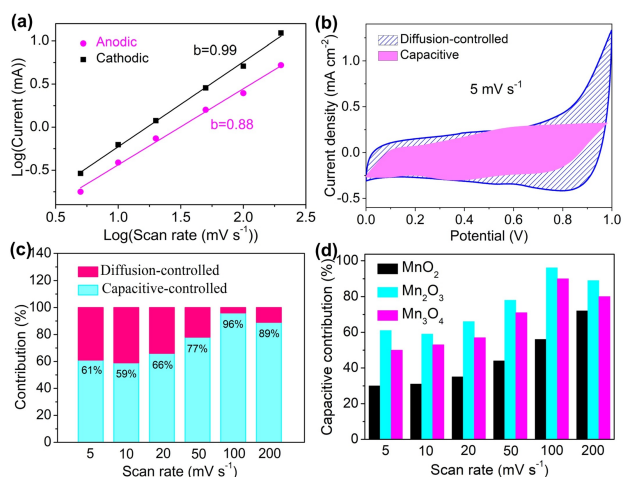


Figure 7. (a) The plots of $\log(i)$ versus $\log(v)$ for Mn_2O_3 electrode. (b) CV curves of the capacitive-controlled and diffusion-controlled processes of Mn_2O_3 electrode at 5 mV s^{-1} . (c) The ratios of the capacitive-controlled and diffusion-controlled charge storage processes at different scan rates. (d) Capacitive contribution of MnO_2 , Mn_2O_3 and Mn_3O_4 electrodes at different scan rates.

ure S3 clearly depict the CV curves of capacitive-controlled and diffusion-controlled processes. The contributions of the capacitive-controlled process were 61%, 59%, 66%, 78%, 96% and 89% at scan rates of 5, 10, 20, 50, 100 and 200 mV s^{-1} , respectively (Figure 7c). Mn_3O_4 electrode also exhibited a capacitive-controlled process with a large percentage range from 50% to 90% (Figure S4 and Figure S6a). MnO_2 electrode demonstrated a low capacitive contribution (less than 50%) at the scan rates range from 5 to 50 mV s^{-1} . When the scan rates increased to 100 and 200 mV s^{-1} , MnO_2 electrode showed a

capacitive-controlled process (Figure S5 and Figure S6b). Additionally, the capacitive contribution of Mn_2O_3 , MnO_2 and Mn_3O_4 electrodes were compared (Figure 7d). Mn_2O_3 electrode demonstrated a higher capacitive contribution than MnO_2 and Mn_3O_4 electrodes. Consequently, these results further confirm that the charge storage process of Mn_2O_3 and Mn_3O_4 is mainly dominated by a capacitive-controlled process.

A symmetric supercapacitor was assembled using two slices of Mn_2O_3 electrodes. The CV curves were performed at 50 mV s^{-1} under different potential windows to estimate the optimum operating voltage of the fabricated symmetric supercapacitor. The device exhibited a stable potential window up to 2.0 V with a slight polarization phenomenon (Figure 8a). Herein, we explored the electrochemical performance of the device at the maximum operating voltage of 2.0 V. The CV curves at various scan rates all exhibited a quasi-rectangular shape, demonstrating the capacitive characteristic (Figure 8b).

The GCD curves of the device at various current densities ranging from 1 to 20 mA cm^{-2} displayed a symmetric triangle shape (Figure 8c), illustrating the excellent reversibility of the symmetric supercapacitor. The device exhibited a high specific capacitance of 210.7 mF cm^{-2} at 1 mA cm^{-2} (Figure 8d). When the current density increased to 20 mA cm^{-2} , the specific capacitance can still reach to 14.3 mF cm^{-2} . Meanwhile, the device showed good coulombic efficiencies at various current densities of nearly 100%. The device exhibited a comparable energy density of 29.3 Wh kg^{-1} at 250 W kg^{-1} to previous reports, such as $\text{MnO}_2\text{-CNT//AC}$ (25 Wh kg^{-1} at 500 W kg^{-1}),^[22] $\text{MnO}_2\text{/CNTs//AC}$ (13.3 Wh kg^{-1} at 600 W kg^{-1}),^[23] $\text{MnO}_x\text{-CSs-600//AC}$ (27.5 Wh kg^{-1} at 225 W kg^{-1}),^[24] $\text{MnO}_2\text{//AC}$ (11.0 Wh kg^{-1} at 50 W kg^{-1}),^[25] birnessite-type $\text{MnO}_2\text{//AC}$ (17.1 Wh kg^{-1} at 100 W kg^{-1}).^[26] Furthermore, the device demonstrated an excellent cycling stability with a capacitance retention of nearly

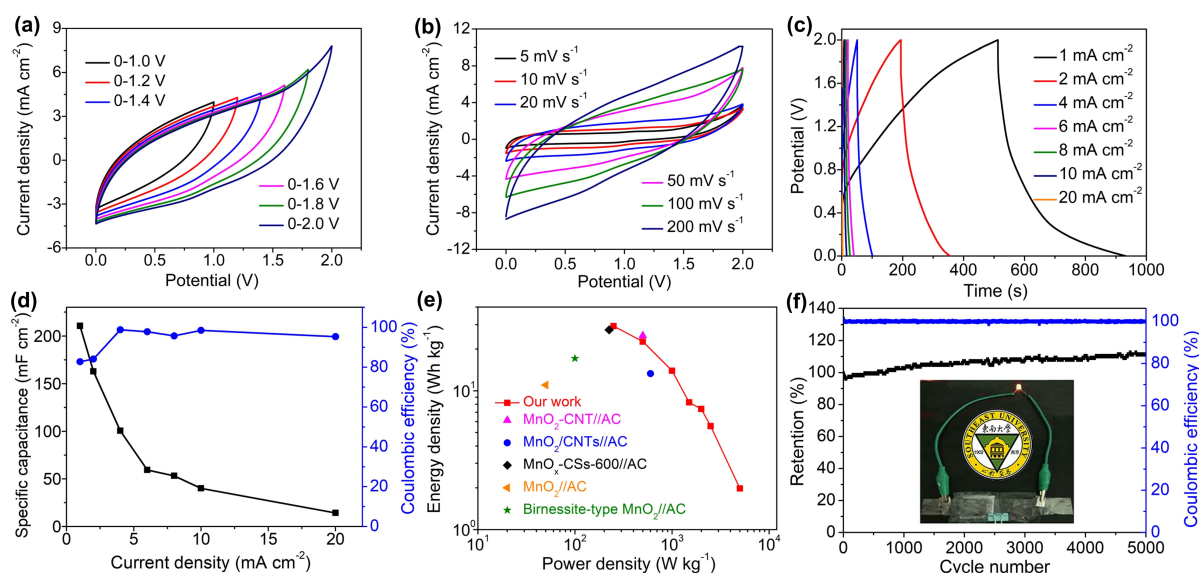


Figure 8. Electrochemical performance of the assembled $\text{Mn}_2\text{O}_3\text{/Mn}_2\text{O}_3$ device: (a) CV curves of the device tested at different potential windows. (b) CV curves of the device at different scan rates. (c) GCD curves of the device at various current densities. (d) Specific capacitances of the device at various current densities. (e) Ragone plots of the device. (f) Cycling stability and coulombic efficiency at 6 mA cm^{-2} for 5000 cycles (Inset: a red LED lightened by two devices connected in series).

100.0% for 6000 cycles at 6 mA cm⁻² (Figure 8f). The coulombic efficiency of the device is nearly 100.0% upon 5000 cycles. A red LED can be lightened up by two devices connected in series. The EIS measurements after the first cycle and 5000th cycle were conducted to analyze the electrochemical kinetics and stability of the device (Figure S7). The device demonstrated a low R_s value of 4.6 Ω cm² after the first cycle. After 5000 cycles, the R_s value and the radius of the semicircle were nearly unchanged. The slope of the straight line at the low frequency region after 5000 cycles slightly decreased. These results indicate the excellent stability of the device during the charge/discharge tests.

Conclusion

In summary, hierarchical MnO₂, Mn_xO_y, Mn₂O₃ and Mn₃O₄ microspheres were prepared by a one-pot hydrothermal method and subsequent annealing processes. Two pairs of Mn³⁺/Mn²⁺ and Mn⁴⁺/Mn³⁺ redox couples were involved in the intercalation/deintercalation of electrolyte ions. The trivalent manganese with Mn³⁺/Mn²⁺ and Mn⁴⁺/Mn³⁺ redox couples can enhance the specific capacitance of Mn₂O₃. Two possible redox reaction equations were proposed to illustrate the charge storage mechanism of sodium cations intercalation/deintercalation processes. The Mn₂O₃ electrode integrated the merits of multiple redox couples, ordered mesoporous structure and large specific surface area, demonstrating excellent electrochemical performance for supercapacitors. The Mn₂O₃ electrode exhibited the maximum specific capacitance of 209.1 F g⁻¹ at 1 A g⁻¹. All the manganese oxide electrodes yielded extraordinary capacitance retentions of over 99.7% after 5000 cycles due to the unique sphere-like structures. The symmetric Mn₂O₃//Mn₂O₃ device yielded a maximum energy density of 29.3 Wh kg⁻¹ at 250 W kg⁻¹. This study will provide an important reference for the future research of manganese oxides.

Experimental Section

Synthesis of hierarchical manganese oxide microspheres: Glucose (0.2 g) and MnSO₄ (2.41 g) were added to distilled water (40 mL) and stirred for 6 h. Then (NH₄)₂S₂O₈ (3.64 g) was added to the above mixture under stirring. The obtained mixture was transferred into a 50 mL autoclave and maintained at 180 °C for 4 h. The resulting suspension was centrifuged and washed with deionized water and ethanol three times. The products were dried at 80 °C overnight to obtain MnO₂ microspheres. Then, MnO₂ microspheres were calcined at 400 °C, 500 °C and 800 °C for 2 h in N₂ atmosphere to obtain Mn_xO_y, Mn₂O₃ and Mn₃O₄ microspheres, respectively.

Materials characterization: The X-ray diffraction (XRD) measurements were conducted on a Shimadzu/ XD-3 A using Cu Kα radiation (λ = 0.15406 nm). The structure and morphology were analyzed by scanning electron microscopy (SEM, JEOL JSM-6700F) and transmission electron microscope (JEOL JEM 200EX). The nitrogen adsorption/desorption measurements were measured on Micromeritics ASAP 2020. The corresponding results were calculated using the Brunauer-Emmett-Teller (BET) and Barrett-Joyner-Halenda (BJH) methods.

Electrochemical tests: The cyclic voltammograms (CV) and galvanostatic charge-discharge (GCD) tests were evaluated by a three-electrode method in 1 M Na₂SO₄ electrolyte. Electrochemical impedance spectroscopy (EIS) was conducted with an amplitude of 5 mV in a frequency range from 0.01 Hz to 100 kHz at open circuit potential. The differential pulse voltammogram (DPV) was tested from 0 to 1 V at different pulse amplitudes. The working electrode was fabricated by mixing manganese oxides, acetylene black and polytetrafluoroethylene (PTFE, 60 wt% dispersion in water) with a weight ratio of 8:1:1. The mixture was coated on a graphite paper (1 cm × 1 cm). The mass loadings of metal oxides on each electrode was around 2.0 mg cm⁻². A Platinum wire (= 1 mm in diameter) and a Hg/HgO electrode were used as the counter and reference electrodes, respectively. The symmetric supercapacitor was assembled by two Mn₂O₃ electrodes using 1 M Na₂SO₄ aqueous solution as the electrolyte. The obtained device was measured in a two-electrode system.

Calculations: The specific capacitance (C_s, F g⁻¹), energy density (E, Wh kg⁻¹) and power density (P, W kg⁻¹) were calculated according to equations (5–7), respectively.^[16]

$$C_s = \frac{I \Delta t}{m \Delta V} \quad (5)$$

$$E = \frac{1}{2 \times 3.6} C \Delta V^2 \quad (6)$$

$$P = \frac{3600E}{\Delta t} \quad (7)$$

where I (A), Δt (s) and ΔV (V) represent the constant discharge current, discharge time and potential window, respectively.

Acknowledgements

This work was financially supported by the National Natural Science Foundation of China (61774033), Scientific Research Foundation of Graduate School of Southeast University (YBYP2153) and Key Laboratory of Water Environment Evolution and Pollution Control in Three Gorges Reservoir (WEPKL2016LL-01, WEPKL2019ZD-03). We also thank the Big Data Center of Southeast University for providing the facility support on the numerical calculations.

Conflict of Interest

The authors declare no conflict of interest.

Keywords: manganese oxide · Mn₂O₃ · redox couple · supercapacitor · trivalent

- [1] W. Wei, X. Cui, W. Chen, D. G. Ivey, *Chem. Soc. Rev.* **2011**, *40*, 1697–1721.
- [2] a) S. Zhu, L. Li, J. Liu, H. Wang, T. Wang, Y. Zhang, L. Zhang, R. S. Ruoff, F. Dong, *ACS Nano* **2018**, *12*, 1033–1042; b) S. Ji, Y. Ma, H. Wang, J. Key, D. J. L. Brett, R. Wang, *Electrochim. Acta* **2016**, *219*, 540–546.
- [3] S. Komaba, T. Tsuchikawa, A. Ogata, N. Yabuuchi, D. Nakagawa, M. Tomita, *Electrochim. Acta* **2012**, *59*, 455–463.

- [4] M. Fu, W. Chen, X. X. Zhu, Q. Y. Liu, *J. Power Sources* **2018**, *396*, 41–48.
- [5] M. J. Cui, S. C. Tang, Y. J. Ma, X. L. Shi, J. A. Syed, X. K. Meng, *J. Power Sources* **2018**, *396*, 483–490.
- [6] E. Saputra, H. Zhang, Q. Liu, H. Sun, S. Wang, *Chemosphere* **2016**, *159*, 351–358.
- [7] B. Jiang, C. Xu, C. Wu, L. Dong, J. Li, F. Kang, *Electrochim. Acta* **2017**, *229*, 422–428.
- [8] J. Cao, J. Li, L. Li, Y. Zhang, D. Cai, D. Chen, W. Han, *ACS Sustainable Chem. Eng.* **2019**, *7*, 10699–10707.
- [9] a) W. Lu, J. Shen, P. Zhang, Y. Zhong, Y. Hu, X. W. Lou, *Angew. Chem. Int. Ed.* **2019**, *58*, 15441–15447; *Angew. Chem.* **2019**, *131*, 15587–15447; b) Y. Qiao, Q. Sun, J. Xi, H. Cui, Y. Tang, X. Wang, *J. Alloys Compd.* **2016**, *660*, 416–422.
- [10] a) Y. Wang, H. Li, Y. Ren, X. Chen, K. Xie, Y. Sun, *Nanotechnology* **2018**, *29*, 385402; b) W. Wang, H. Bi, C. Li, J. Zhang, J. Feng, Y. Wang, X. Huang, Y. Sun, L. Sun, *Mater. Today Nano* **2019**, *6*, 100033; c) Y. Wang, S. Wang, Y. Wu, Z. Zheng, K. Hong, B. Li, Y. Sun, *Electrochim. Acta* **2017**, *246*, 1065–1074.
- [11] H. She, Y. Sun, S. Li, J. Huang, L. Wang, G. Zhu, Q. Wang, *Appl. Catal. B* **2019**, *245*, 439–447.
- [12] X. Gu, J. Yue, L. Li, H. Xue, J. Yang, X. Zhao, *Electrochim. Acta* **2015**, *184*, 250–256.
- [13] G. Wang, H. Xu, L. Lu, H. Zhao, *J. Mater. Chem. A* **2015**, *3*, 1127–1132.
- [14] T. L. Silva, A. Ronix, O. Pezoti, L. S. Souza, P. K. T. Leandro, K. C. Bedin, K. K. Beltrame, A. L. Cazetta, V. C. Almeida, *Chem. Eng. J.* **2016**, *303*, 467–476.
- [15] Q. Zhang, M. D. Levi, Q. Dou, Y. Lu, Y. Chai, S. Lei, H. Ji, B. Liu, X. Bu, P. Ma, X. Yan, *Adv. Energy Mater.* **2019**, *9*, 1802707.
- [16] a) H. Darjazi, S. S. Hosseiny Davarani, H. R. Moazami, T. Yousefi, F. Tabatabaei, *Prog. Nat. Sci.: Met. Mater. Int.* **2016**, *26*, 523–527; b) Z.-Y. Li, M. S. Akhtar, P. T. M. Bui, O. B. Yang, *Chem. Eng. J.* **2017**, *330*, 1240–1247.
- [17] a) P. Du, W. Wei, D. Liu, H. Kang, P. Liu, *Chem. Eng. J.* **2018**, *335*, 373–383; b) T. T. Jiang, S. Y. Yang, Z. M. Bai, P. Dai, X. X. Yu, M. Z. Wu, H. B. Hu, *Nanotechnology* **2018**, *29*, 315402.
- [18] N. Wang, H. Song, H. Ren, J. Chen, M. Yao, W. Huang, W. Hu, S. Komarneni, *Chem. Eng. J.* **2019**, *358*, 531–539.
- [19] S. Kandula, K. R. Shrestha, N. H. Kim, J. H. Lee, *Small* **2018**, *14*, 1800291.
- [20] X. Chen, D. Jiang, H. Li, K. Xie, Y. Jiang, Y. Wang, *J. Colloid Interface Sci.* **2020**, *575*, 168–176.
- [21] J. Jiang, Z. Li, X. He, Y. Hu, F. Li, P. Huang, C. Wang, *Small* **2020**, *16*, 2000180.
- [22] F. Ochai-Ejeh, M. J. Madito, K. Makgopa, M. N. Rantho, O. Olaniyan, N. Manyala, *Electrochim. Acta* **2018**, *289*, 363–375.
- [23] L. Li, Z. A. Hu, N. An, Y. Y. Yang, Z. M. Li, H. Y. Wu, *J. Phys. Chem. C* **2014**, *118*, 22865–22872.
- [24] S. Chen, D. Cai, X. Yang, Q. Chen, H. Zhan, B. Qu, T. Wang, *Electrochim. Acta* **2017**, *256*, 63–72.
- [25] K. B. Hatzell, L. Fan, M. Beidaghi, M. Boota, E. Pomerantseva, E. C. Kumbur, Y. Gogotsi, *ACS Appl. Mater. Interfaces* **2014**, *6*, 8886–8893.
- [26] X. Zhang, P. Yu, H. Zhang, D. Zhang, X. Sun, Y. Ma, *Electrochim. Acta* **2013**, *89*, 523–529.

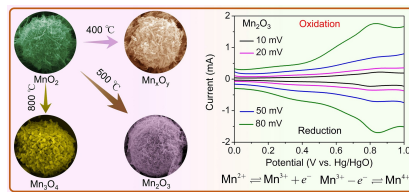
Manuscript received: January 11, 2021

Accepted manuscript online: March 29, 2021

Version of record online: ■■■, ■■■■

FULL PAPER

Effect of manganese valence on specific capacitance: Hierarchical manganese oxides microspheres were prepared by hydrothermal and calcination methods. Mn_2O_3 exhibited $\text{Mn}^{3+}/\text{Mn}^{2+}$ and $\text{Mn}^{4+}/\text{Mn}^{3+}$ transitions during the charge/discharge process. The redox reaction equations of Mn_2O_3 was proposed based on the electrochemical measurements. Mn_2O_3 exhibited superior specific capacitance due to the two redox couples and unique structure.



*Dr. X. Chen, L. Li, Dr. X. Wang, Prof. K. Xie, Prof. Y. Wang**

1 – 9

Effect of Manganese Valence on Specific Capacitance in Supercapacitors of Manganese Oxide Microspheres

